EMT-NH 2 zeolite nanocrystal interlayer induces the formation of high-performance polyamide membrane with heterogeneity morphology

Shengchao Wei, Yaoli Guo, Ge Yang, Hailing Guo, Zifeng Yan, Svetlana Mintova, Q. Jason Niu

EMT-NH_2 zeolite nanocrystal interlayer induces the formation of high-performance polyamide membrane with heterogeneity morphology

Sheng-Chao Wei[a], Yao-Li Guo[a, b], Ge Yang[a], Hai-Ling Guo[a*], Zi-Feng Yan[a,]

Svetlana Mintova[a, c], Q. Jason Niu[a, b*]

[a] State Key Laboratory of Heavy Oil Processing, College of Chemical Engineering, China University of Petroleum (East China), Qingdao 266580, China.

[b] Institute for Advanced Study, Shenzhen University, 518060, China

[c] Normandie Universite, ENSICAEN, UNICAEN, CNRS, Laboratoire Catalyse et Spectrochimie (LCS), 14050 Caen, France

* Corresponding author.

Hai-Ling Guo's Email: guohl@upc.edu.cn

Q. Jason Niu's Email: qjasonniu@szu.edu.cn

ABSTRACT

Conventional nanofiltration (NF) thin-film composite (TFC) membranes are strongly restricted by the trade-off between their water permeance and selectivity as well as the poor structural stability for desalination and wastewater treatment. Herein, we report an interlayer-based thin-film composite (i-TFC) NF membrane with high performance using amino-functionalized EMT zeolite (EMT-NH_2) nanocrystals as the interlayer. By adjusting the distribution density of EMT-NH_2 on the substrate, a thin and dense PA layer with heterogeneity multi-level morphology (nanosized nodules and nanoscale stripes) can be formed and regulated. The EMT-NH_2 zeolite nanocrystals with numerous hydrophilic groups (hydroxy and amino groups) and internal cavities can provide an additional priority water channel, increase the amine monomer storage on the substrate, and slow down the diffusion of amine monomer, thereby leading to the construction of a dense PA layer with high performance. As a result, the i-TFC-15 membrane depicted a water permeability of 13.82 ± 0.47 L m^{-2} h^{-1}·bar^{-1} (2.5 times that of the controlled one), while maintaining an excellent retention ability for divalent salts (98.55% for Na_2SO_4, 98.42% for $MgSO_4$ and 97.40% for $MgCl_2$). Additionally, the rigid hydrophilic interlayer containing zeolite nanocrystals endowed the i-TFC-15 membrane with excellent pressure resistance (up to 2.4 MPa), long-term operating stability, and antifouling propensity (flux-recovery ratio, 90.1%). This work provides an approach for fabricating a novel high-performance NF membrane and deepens our understanding of the role of porous interlayer affecting the formation of the PA layer.

36 **KEYWORDS**

37 Interfacial polymerization; Zeolite nanocrystal; Interlayer; Thin-film composite membrane

1. Introduction

Membrane-based separation, as a low-energy consumption technology, plays a vital role in solving the challenge of global water scarcity[1, 2]. Especially, the nanofiltration (NF) membrane with thin-film composite (TFC) structure has attracted much attention in municipal water, brackish water desalination, and drinking water treatment due to its high energy efficiency, low-cost effectiveness, and scalable operation[3, 4]. Although some improvements in the NF membrane's performance have been achieved, the conventional TFC NF membranes are still constrained in the large-scale application by the trade-off between their water flux and the desalination rate[5]. In addition, the poor structural stability of NF TFC membranes also inhibits the further improvement of membrane performance. And it is well known that the performance of the TFC membrane is associated with the formation of polyamide (PA) separation layer fabricated by interfacial polymerization[6, 7]. Constructing thinner PA layer structures and nanostructure surface morphologies with internal voids for the PA layer have proven to be effective strategies to reduce water transfer resistance and promote membrane permeability[8]. In the regulation of the PA layer for NF TFC membrane structure, various strategies including monomer design[3, 9], additives additions to the aqueous or oil phase[10, 11], surface modification[12, 13], and interlayer construction on the substrate[14, 15], have been employed to regulate the structure and morphology for PA layer. Among them, simply introducing interlayers on the substrate before the IP process has been proven to be an effective approach to tailoring the structure and morphology of the PA layer. The interlayer can modulate the hydrophobicity, porosity, and surface geometries of the substrate, thereby

regulating the IP process, which is promising to weaken the trade-off restriction and improve the membrane structural stability[14, 16].

Since Livingston fabricated a sub-10nm and defect-free PA layer with unprecedented performance via the construction of a sacrificial layer of Cd $(OH)_2$ nanostrand[17], a slate of organic materials (e.g., polydopamine, tannic, and polymers) and crystal nanomaterials with O-D, 1-D, 2-D, and 3-D structure have been used to construct interlayers[18-21]. Among them, the organic material as interlayer due to the high hydrophobic and high density limited the membrane permeability. While the porous crystal nanomaterials as interlayers were identified as effective in regulating the storage and diffusion of amine monomer during the IP process to improve the performance of membrane[22-24]. In previous work, we fabricated a ZIF-8 interlayer on the surface of non-porous polypropylene to optimize the porosity of the substrate surface and improve the adsorption and storage of amine monomer, forming a defect-free PA layer through the IP process[25]. In addition, an HKUST-1 interlayer on a polyimide substrate was constructed by the *in-situ* growth. The HKUST-1 interlayer as a container for PIP monomer reduced the diffusion coefficient of the PIP monomer due to the linkage between HKUST-1 and PIP monomer, thereby forming a thinner PA layer with fewer defects[26]. However, these MOFs also possess some inherent restrictions and disadvantages. Firstly, the MOFs composed of toxic heavy metal ions and ligands in the TFC membrane are possible to leach in the filtration process, harming the environment and human health[27]. Secondly, the MOFs are generally prepared via complex and high-cost solvothermal methods, which restricts the practical application of the TFC membrane[28]. Zeolite nanocrystals, as

ultrasmall silica-aluminate crystalline materials, are increasingly explored for developing high-performance NF membranes due to their small pore sizes (0.3-1.0 nm), high specific surface areas, adjustable surface properties, and suitable large-scale production[16]. Recently, Zhang fabricated thin-film nanocomposite (TFN) membranes with hierarchical AFI molecular sieves (0.2-1.0 μm) by vacuum filtration[29]. The obtained TFN membrane exhibited excellent water permeability, nearly twice that of the controlled membrane. However, the agglomeration tendency and poor compatibility of nanosized zeolite in NF membrane were prone to cause an unfavorable separation performance and the detachment of the PA layer in practical application. Thus, constructing a porous zeolite interlayer in i-TFC membranes with excellent stability and suitability and exploring its effect on i-TFC membranes is necessary for practical applications.

Herein, a novel i-TFC membrane with heterogeneity multi-level morphology was fabricated using amino-functionalized zeolite nanocrystals as interlayers. The ultrasmall-sized (15-20 nm) amino-functionalized EMT-NH_2 nanocrystals on an amino-modified substrate enhanced the compatibility and interfacial interactions of the zeolite interlayer in the TFC membrane. And the constructed EMT-NH_2 nanocrystal interlayer improved the water permeability (almost 2.5 times that of the controlled one) and retention ability of divalent salts of the i-TFC membrane caused by the additional priority water channels and the regulated structure and morphology of the PA layer. Furthermore, the i-TFC membranes with rigid and hydrophilic zeolite nanocrystal interlayers possessed enhanced pressure resistance, long-term

stability, and antifouling propensity, which contributes to maximizing the water flux of i-TFC membranes in practical applications.

2. Materials and methods

2.1. Chemicals and materials

Sodium hydroxide (NaOH, AR, ≥96%), Hydrochloric acid (HCl, AR, 36-38%), Sulfuric acid (H_2SO_4, AR, 95-98%), Sodium aluminate ($NaAlO_2$, CP), Zinc powder (AR, ≥95%), ethanol (AR, ≥99.7%), Bovine Serum Albumin (BSA, BR), Polyethylene glycol (PEG, CP, molecular weight: 200, 300, 400, 600, 800, 10000, 20000, 40000, 70000, and 100000), and other chemicals including $NaNO_2$ (AR, ≥99%), Na_2SO_4 (AR, ≥99%), $MgSO_4$ (AR, ≥98%), $MgCl_2·6H_2O$ (AR, ≥98%), $CaCl_2$ (AR, ≥96%), NaCl (AR, ≥99.5%), LiCl (AR, ≥97%) were purchased from Sinopharm Chemical Reagent Co., Ltd (China). Sodium silicate (26.5% SiO_2, 8.3% Na_2O) was acquired from Yousuo Chemical Technology Co., Ltd (China). Piperazine (PIP, GC, ≥98%), P-Phenylenediamine (PPD, GC, ≥98%), and Trimesoyl chloride (TMC, GC, ≥98%) were purchased from TCI (Japan). The polysulfone (PSF) ultrafiltration membrane employed as the support substrate was obtained from OriginWater Technology Co., Ltd (Beijing, China). To remove the stains and pollutants in the PSF membrane hole, the PSF membranes were soaked in ethanol solution with a concentration of 50% for 1 h, and then transferred to the deionized (DI) water soaked for 6 h before use. The DI water used was provided by a secondary RO purification device.

2.2. Preparation of the NF membranes

2.2.1. Preparation of EMT-NH_2 zeolite nanocrystal

According to the previous study[30], the EMT zeolite nanocrystal (diameter of 15-20 nm) was synthesized via low-temperature hydrothermal method without organic structural direction agent. The molar composition of zeolite gel was 7.86 SiO_2: 1 Al_2O_3: 26.72 Na_2O: 389.97 H_2O. And the synthesis procedure of EMT zeolite nanocrystal was performed as follows: 0.41 g of NaOH was added to 25.00 g of H_2O with stirring for 5 min, together with 2.05 g of $NaAlO_3$ and stirred vigorously. Then, 11.12 g of NaOH was added to the above aqueous solution with stirring for 4 h to obtain the solution A. Solution B was prepared by dissolving 2.95 g of NaOH in 20.00 g of H_2O followed by slow addition of 14.70 g of sodium silicate with stirring for 4 h. Subsequently, the solution A was added dropwise to the solution B under stirring and obtain the initial suspension. During the mixing, the solution A and B were kept in ice. After mixing, the resulting suspension was aged with stirring for 30 min at room temperature (~25℃). Finally, the obtained suspension was transferred into a water-bath at 35℃ for 36 h to crystallize. The crystallized products were separated through centrifugal and repeatedly washed with DI water until the solution was neutral. And the collected samples were denoted as EMT zeolite nanocrystal. The crystal structure and chemical structure for EMT zeolite with different crystal times were initial characterized through XRD and FT-IR (Fig. S1). And the EMT with 20 h crystallization was selected for constructing interlayer due to its better crystallization degree and greater content of silicon-hydroxyl groups. In addition,

it should be noted that the ultra-small EMT zeolite nanocrystal was dispersed by the wet method, which avoids its aggregation.

According to the procedure reported by our group[12], the diazonium aqueous solution was prepared as follows (Fig. S2): 1.38 g of $NaNO_2$ was added to 200 mL of H_2O with stirring vigorously to dissolve completely. And 2.16 g of P-Phenylenediamine (PPD) was added to 200 mL of HCl aqueous solution (0.5 mol/L). Then, the $NaNO_2$ aqueous solution was slowly added dropwise to the above PPD aqueous solution to obtain a mixed solution followed by slow addition of 4.00 g of Zn powder to transform aryldiazonium to aryl radicals. After adding Zn powder, the resulting mixed solution was filtered twice with 0.20 μm of microfiltration membrane. After filtering, the filtrate was separated by high-speed centrifugation (10000 rpm, 20 min) and obtained the diazonium solution. The chemical structure of diazonium solution (containing diazonium salt cationic radicals, aryl cationic radicals, and partial grafted aryl diazonium salts) was determined by FTIR spectra (Fig. S3). And the concentration of prepared diazonium solution was 0.05 mol/L.

The amino-functionalized EMT (denoted as EMT-NH_2) zeolite is prepared as follows: 100 ml of fresh diazonium aqueous solution (0.05 mol/L) was mixed with 100 mL of EMT aqueous solutions (0.1wt%), followed by stirring at room temperature (25℃) for 5 h. Then, the solid products were separated and washed by high-speed centrifugation (10000 rpm, 20 min) with ethanol repeatedly. Finally, the obtained product was dispersed in water to obtain the EMT-NH_2 aqueous solution. The concentration of EMT-NH_2 aqueous solution was determined by evaporating the solvent EMT-NH_2 aqueous solution.

2.2.2. Preparation of zeolite interlayer on substrates

The zeolite interlayer on the substrate (denoted as MPSF-EMT) was prepared as follows: Firstly, 30 mL of fresh diazonium solution was deposited on the PSF substrate fixed by a frame (40 cm^2 of area) for 2 h to obtain the modified MPSF substrate. Then, the MPSF substrate was washed repeatedly with DI water and stored in DI water for 12 h before use. After that, 30 mL of EMT-NH_2 zeolite aqueous solution (0.001 wt%) was deposited on the MPSF substrate mounted on a frame. After deposition for different times (5, 10, 15, and 20 h), the EMT-NH_2 aqueous solution on MPSF substrate surface was poured off and the MPSF-EMT substrates with zeolite interlayer was obtained. And the obtained MPSF-EMT substrates were transferred into the DI water for 1 h to remove the unstable zeolite nanocrystal. The MPSF-EMT substrates of different deposition times (5, 10, 15, and 20 h) for interlayer were denoted as MPSF-EMT-5, MPSF-EMT-10, MPSF-EMT-15, and MPSF-EMT-20, respectively.

2.2.3. Preparation of NF membranes with zeolite interlayers

The i-TFC membranes with zeolite interlayers were prepared via the IP process on the MPSF-EMT substrate (Scheme 1)[31]. Firstly, the MPSF-EMT substrate was fixed in the plastic frame (area is 40 cm^2) and then immersed in the 30 mL of PIP aqueous solution (1wt%). After immersing for 2 min, the residual solution on the substrate surface was removed using the roller. Then 30 mL of TMC n-hexane solution (0.1wt%) was poured on the surface of MPSF-EMT substrates to react with PIP monomer. After reacting for 30 s, the TMC

n-hexane solution was poured off and the obtained the PA layer was rinsed with pure n-hexane for 6 s. Subsequently, the obtained i-TFC membrane was transferred into an oven at 60℃ for 2 min to facilitate the cross-linking of the PA layer. After drying, the fabricated membrane is transferred into DI water before use. The NF TFC membrane directly constructed on PSF and MPSF substrates via the IP process were denoted as TFC and MTFC, respectively. And the TFC NF membranes fabricated on MPSF-EMT-5, MPSF-EMT-10, MPSF-EMT-15, and MPSF-EMT-20 substrates were denoted as i-TFC-5, i-TFC-10, i-TFC-15, and i-TFC-20, respectively.

2.3. Evaluation of NF performance

The performance tests of membranes were performed in a crossflow filtration system with eight filtration units (each unit area is 28.5 cm^2). The operating pressure and temperature were controlled at 1 MPa and 25℃. The concentration of all salt solutions (Na_2SO_4, $MgSO_4$, $MgCl_2$, $CaCl_2$, NaCl, and LiCl) was 2000 μg/g[32]. To obtain accurate results, the membrane was pre-compacted at 1 MPa before testing. After compaction for 1 h, the permeate water was collected three times and the average value was recorded. The concentration of the salt solution was obtained by using the conductivity meter (Mettler Toledo FiveEasy Plus, Switzerland). The water permeance (J, $L \cdot m^{-2} \cdot h^{-1} \cdot bar^{-1}$) of NF membranes is calculated by equation (1).

$$J_w = V/(A \cdot \Delta t \cdot \Delta P) \quad (1)$$

Of which V (L) is the permeate volume, A (m^2) is the effective membrane area, Δt (h) and

200 ΔP (bar) are the operating time and pressure, respectively. The salt rejection for NF
201 membranes was calculated by equation (2).

202 $$R=(1-C_p/C_f)\times 100\% \quad (2)$$

203 Here, R represents the salt rejection. C_p and C_f are the solute concentrations in permeate
204 and feed, respectively.

205 The PEG rejection curves of the membranes and substrates were determined via solute
206 transport method[33]. The 200 μg/g of PEG (MW: 200, 300, 400, 600, and 800) solutions as
207 feedstock solutions were filtrated at 0.6 MPa to explore the pore structure of NF
208 membranes[33]. And the 200 μg/g of PEG (MW: 10000, 20000, 40000, 70000, and 100000)
209 solutions as feedstock solutions were filtrated at 0.6 MPa to explore the pore structure of
210 modified PSF substrates. The concentrations of PEG solutions were obtained using total
211 organic carbon analyzer (Shimadzu, TOCL CPH), and the PEG rejection was calculated on
212 equation (3). The molecular weight corresponding to the 90% rejection is defined as
213 molecular weight cut-off (MWCO). In addition, the Stokes radius ds (nm) of PEG was
214 calculated according to equation (4). And the Stokes radius corresponding to MWCO is
215 defined as the effective pore size of the membranes and substrates.

216 $$R=(1-TOC_p/TOC_f)\times 100\% \quad (3)$$

217 Of which, R represents the PEG rejection, TOC_p and TOC_f represent the solute
218 concentration in the permeate and feedstock solutions, respectively.

219 $$ds=33.46\times 10^{-3}\times M^{0.557} \quad (4)$$

220 Of which, M represents the PEG molecular weight.

2.4. Antifouling filtration and chemical stability test

The antifouling properties of fabricated membranes were studied by filtrating BSA solution[34]. All membranes were pre-compacted at 1 MPa for 1 h before testing to obtain a stable pure water flux (labeled as J_0, $L \cdot m^{-2} \cdot h^{-1}$). Then, the feedstock solution was changed to 500 μg/g of BSA solution for 6 hours of filtrating at 1 MPa (The final water flux was denoted as J_1 ($L \cdot m^{-2} \cdot h^{-1}$)). After 6-hour filtrating, the membrane was rinsed using DI water. After 3 hours of rinsing, the membranes were filtrated with DI water for 2 h to obtain a stable water flux of J_2 ($L \cdot m^{-2} \cdot h^{-1}$). Based on equations (5) and (6), the flux-decline ratio (FDR) and the flux-recovery ratio (FRR) were obtained[35].

$$FDR=(1-J_1/J_0)\times 100\% \quad (5)$$

$$FRR=J_2/J_0\times 100\% \quad (6)$$

The chemical stability test of fabricated membranes was investigated via immersing membranes in H_2SO_4 aqueous solution (pH=3), pure aqueous solution (pH=7), and NaOH aqueous solution (pH=10) for 24 h, respectively. Before performance evaluation, all immersed membranes must be rinsed completely using DI water.

2.5. Characterization of NF membranes

The chemical properties and crystal structure of the zeolite nanocrystal were analyzed by Fourier transform infrared spectroscopy spectra (FTIR, Bruker Vertex, USA) and X-ray diffraction (XRD, Bruker D8 Advance, USA). The morphologies and size of zeolites were measured using a TEM (FEI Tecnai F20, USA). The pore structure of the zeolite nanocrystal

was analyzed by the N_2 adsorption isotherms (Micromeritics ASAP 2020). The surface charge properties of zeolites were determined by a nanoparticle analyzer (Zeta, SZ-100-Z, HORIBA, Japan). The chemical structures and cross-linking structure of NF membranes were analyzed by ATR-FTIR (Thermo Fisher Scientific, Nicolet iS20, USA) and XPS (Thermo Fisher Scientific, USA). The surface morphology of substrates and membranes were analyzed on a Field-emission SEM (JEOL-7900F, Japan). Energy dispersive spectroscopy (EDS) of zeolite nanocrystal was performed on an EDAX XM2-30T apparatus. The surface roughness of NF membranes was analyzed on AFM (Shimadzu SPM-9700, Japan). The relative content of piperazine in hexane solution was measured by a UV-visible spectrophotometer (UV-vis, Shimadzu UV-2450, Japan). The surface charges and surface wettability of substrates and NF membranes were investigated on the streaming potential analyzer (Aaton-Paar SurPASS3, Austria) and a drop shape analyzer (Krüss DSA25, Germany), respectively.

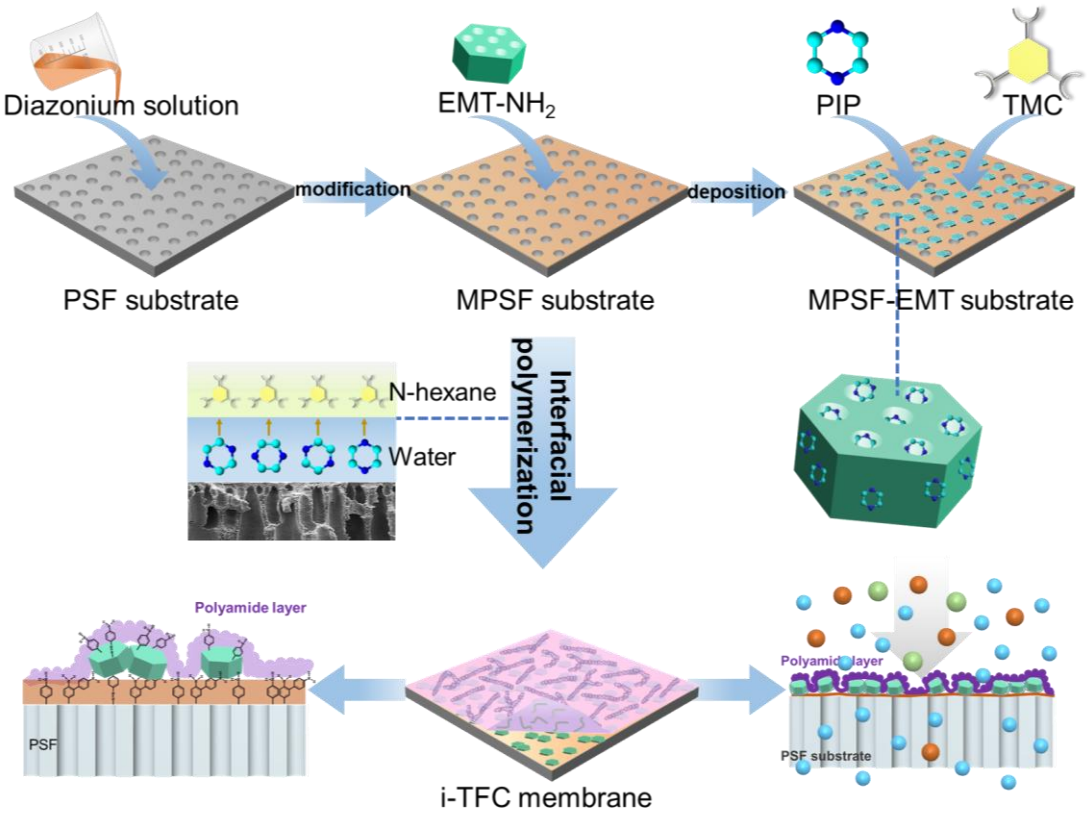

Scheme 1. Schematical illustration regarding the fabrication process of i-TFC membranes with zeolite nanocrystal interlayer

3. Results and discussions

3.1. Characterization of EMT-NH_2 zeolite nanocrystal interlayers

The ultra-small EMT zeolite was synthesized via a low-temperature hydrothermal method and was further modified with diazonium reaction (Fig. 1a-b). The FTIR spectra (Fig. 1c) of EMT-NH_2 contains the characteristic absorption peaks of aniline groups (ν(-Ar) 1515 cm^{-1}; ν(N-H) 3370 cm^{-1}), determining the existence of amino group[36, 37]. XPS analysis (Fig. 1d and Fig. S4) shows the peaks of -NH_2 (at 399.8 eV, 35.4%) and -N=N- (at 402.1 eV, 64.6%) in fitting results of N1s XPS spectra for EMT-NH_2, further confirming that the amino group was

264 introduced successfully in EMT-NH_2 nanocrystals[29]. In addition, the color variation (from
265 colorless to brown) of the zeolite solution and zeolite powder also prove the successful
266 preparation of amino-functionalized EMT nanocrystals (Fig. S5). The excellent hydrophilicity
267 of zeolite nanocrystals was demonstrated by the fact that the zeolite solution remained
268 homogeneous after 24 hours of standing. The introduced amino groups partially destroyed the
269 crystal structure of EMT-NH_2 nanocrystals, whereas the EMT-NH_2 still maintains part of the
270 EMT-type zeolite structure, as evidenced by the three characteristic peaks (5.86°, 6.20°, and
271 6.68°) in the enlarged areas of the XRD patterns of EMT-NH_2 (Fig. S6**)**. Besides, the crystals
272 structure with lattice fringes in TEM images of EMT-NH_2 and double-6-ring species (D6R) in
273 the FTIR spectra of EMT-NH_2 further demonstrate the partial EMT-type crystal skeletal
274 structure for EMT-NH_2 (Fig. S7)[38]. Both EMT and EMT-NH_2 exhibit a combination of type
275 I and type IV isotherms due to their micropores and textural mesopores(Fig. S8)[38].
276 Compared with that of EMT, the BET surface area of EMT-NH_2 nanocrystal deceased to
277 381.12 m^2 g^{-1}, whereas EMT-NH_2 nanocrystal possesses a large and homogeneous
278 inter-crystalline mesopore [39]. Despite the introduction of amino groups can disrupt the
279 crystal structure of partial EMT-NH_2 zeolite nanocrystals to some extent, the EMT-NH_2
280 zeolite still maintains the structural characteristics of EMT-type zeolite. In addition, the zeta
281 potentials of EMT and EMT-NH_2 solution at pH=7 are -33.8 mV and -21.3 mV, respectively,
282 meaning that the diazonium reaction weakens the electronegativity (Fig. 1f). Compared with
283 that of EMT nanocrystal, the peak strength of Na element at 1071 eV in the EMT-NH_2
284 nanocrystal weakened significantly (Fig. S9), which is consistent with the EDS results (Fig.

S10). In addition, the N elemental as a marker for the diazonium cation can be clearly seen in EMT-NH_2 nanocrystal. The decrease of Na element content and presence of N element in EMT-NH_2 nanocrystal demonstrate that the successful preparation of EMT-NH_2 nanocrystal is carried out by ion exchange between aromatic-base cation and Na^+ ions of zeolites[40].

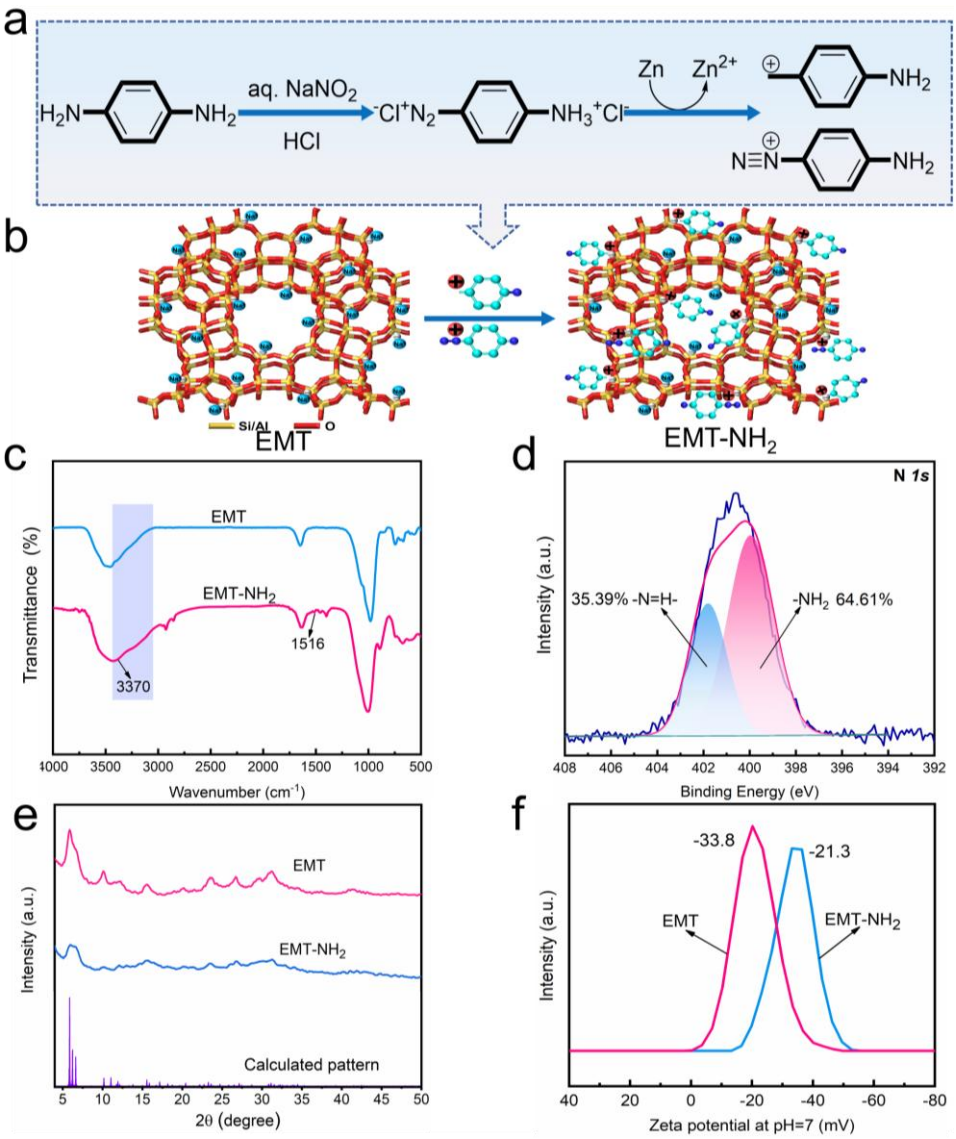

Fig. 1. (a) Schematic diagram of the diazonium reaction; (b) Mechanism of EMT zeolite modified by diazonium solution via ions exchanges; (c) FT-IR spectra of EMT and EMT-NH_2 zeolites; (d) N1s XPS spectra of EMT-NH_2 (e) XRD patterns of EMT and EMT-NH_2 zeolites; (f) Zeta potential curves of EMT and EMT-NH_2 solution

Firstly, the substrates were modified through the diazonium reaction to enhance their hydrophilicity[12]. Subsequently, the EMT-NH_2 solution was deposited on the modified substrate to obtain a stable assembled zeolite interlayer. As depicted in Fig. 2a, two additional peaks (ν(N-H), 3379 cm^{-1}; ν(-NH_2), 1540 cm^{-1}) appeared in the FT-IR spectra of MPSF-EMT substrates, indicating that the amino group is successfully introduced on the MPSF-EMT substrates. The surface negative charges of the MPSF-EMT substrates decrease as confirmed by the increased zeta potential (Fig. 2b). Meanwhile, the isoelectric point of PSF, MPSF, and MPSF-EMT-15 substrate are pH=3.61, pH=4.85, and pH=5.12, respectively (Fig. 2b and Fig. S11), further confirming that the interlayer can weaken the electronegativity of the substrate. Furthermore, the surface hydrophilicity of the MPSF-EMT substrate was acquired via water contact angles (CA) and pure water fluxes in Fig. 2c and Fig. 2d, respectively. For PSF and MPSF-EMT-15, the water contact angles are 70° and 42°, respectively, which verifies that the amino groups and hydrophilic interlayer improve the substrate's hydrophilicity. However, the pure water flux of MPSF-EMT decrease due to the reduction of holes on the surface of the substrate, which is in accordance with the previous literature[12]. The molecular weight cut-offs (MWCO, also known as molecular weight) and effective pore size of the PSF and MPSF-EMT substrates were measured by solute transport method and given in Fig. S12[33]**.** After inserting EMT-NH_2 interlayer, the MWCO and effective pore size of MPSF-EMT substrates tend to be smaller, indicating that the introduced EMT-NH_2 nanocrystal can blocks the surface pores of the substrate. Furthermore, the surface morphology for PSF and MPSF-EMT substrates was analyzed by SEM (Fig. S13). The PSF substrate exhibits a flat

morphology with abundant holes, while the zeolite nanocrystals can be seen on the MPSF-EMT substrate surface. With the prolongation of deposition time, the zeolite interlayer on the PSF surface becomes denser and the visible surface pores of the MPSF-EMT substrate gradually disappear. Herein, the introduction of the zeolite EMT-NH_2 interlayer can reduce the electronegativity, enhance the hydrophilicity, and optimize the pore distribution for the substrate. More importantly, the enhanced hydrophilicity and the enriched pore structure of the substrate surface facilitate the storage of amine monomers, thereby effectively optimizing the IP process.

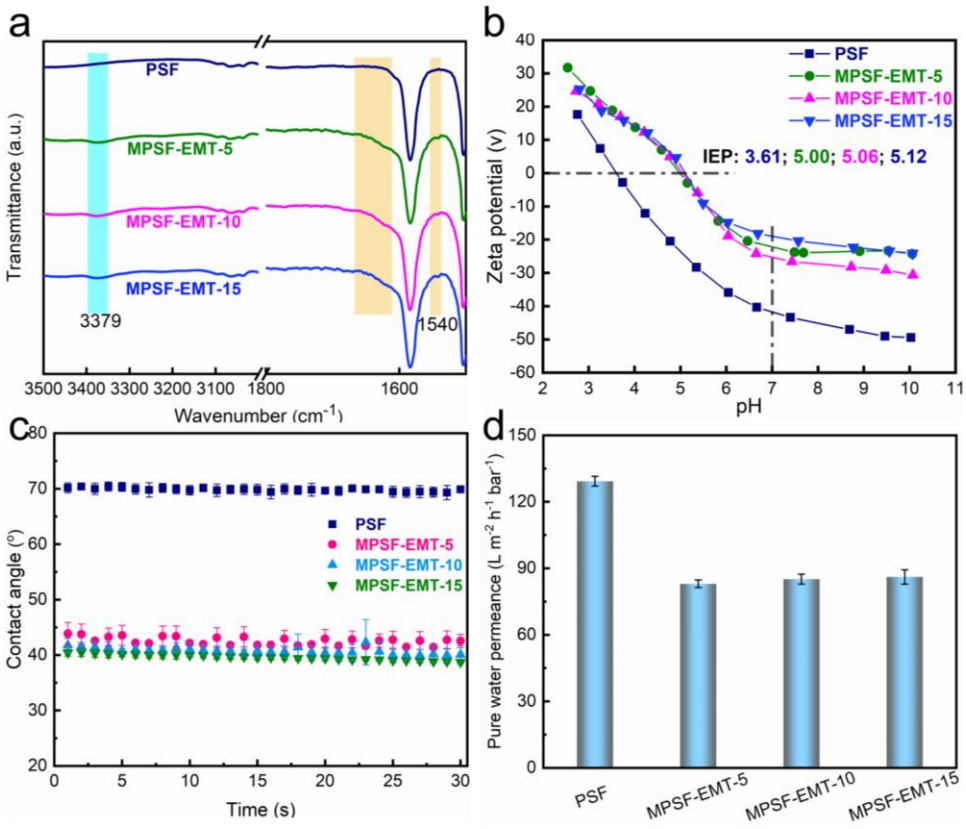

Fig. 2. (a) ATR-FTIR spectra; (b) Surface zeta potential; (c) Water contact angles; and (d) Water fluxes for PSF and MPSF-EMT substrates

3.2. Structural characteristics and surface properties of NF membranes

The ATR-FTIR and XPS analysis for NF membranes with/without interlayer were performed for investigating the functional groups and cross-linking degree of NF membranes. The ATR-FTIR spectra of i-TFC membranes (Fig. 3a) show that there are two distinct absorption peaks at 1622 and 3200-3600 cm^{-1} appeared, which are contributed by the stretching vibration of -C=O and N-H of the amide groups[41]. Such results verify the fabrication of the PA layer on substrate. Interestingly, compared with that of the controlled one, the peak intensity of amide groups for i-TFC membranes enhanced evidently, suggesting that i-TFC membranes possess more amide groups. In addition, the fitting curves (Fig. 3c-f) of the O1s for TFC and i-TFC membranes show that two peaks are observed at 530.2 and 532.5 eV, representing the N-C=O bond of the amide groups and O-C=O bond of the carboxyl groups, respectively[17, 42]. The N-C=O bond content of the i-TFC membrane is higher than that of the controlled one, which further indicates that the i-TFC membrane possesses more amide groups. Thus, it can be reasonably inferred that the MPSF-EMT substrates can supply more PIP monomers to react with TMC, reducing the hydrolysis of TMC and forming more amide groups[42]. Usually, the abundant amide groups are accompanied by a higher cross-linking degree for the PA layer[12]. Table 1 shows that the O/N ratio of i-TFC membranes decreases from 1.70 of TFC to 1.59 of i-TFC-5, 1.43 of i-TFC-10, and 1.42 of i-TFC-15[43]. Furthermore, the cross-linking degrees of i-TFC-5, i-TFC-10, and i-TFC-15 are 31.67%, 46.91%, and 47.94%, respectively, which are higher than that of the controlled membrane (22.22%)[17]. Compared with the PSF substrate, the modified PSF substrates with

interlayer can provide more PIP monomers to participate in the IP process, which leads to the IP reaction between PIP and TMC more completely.

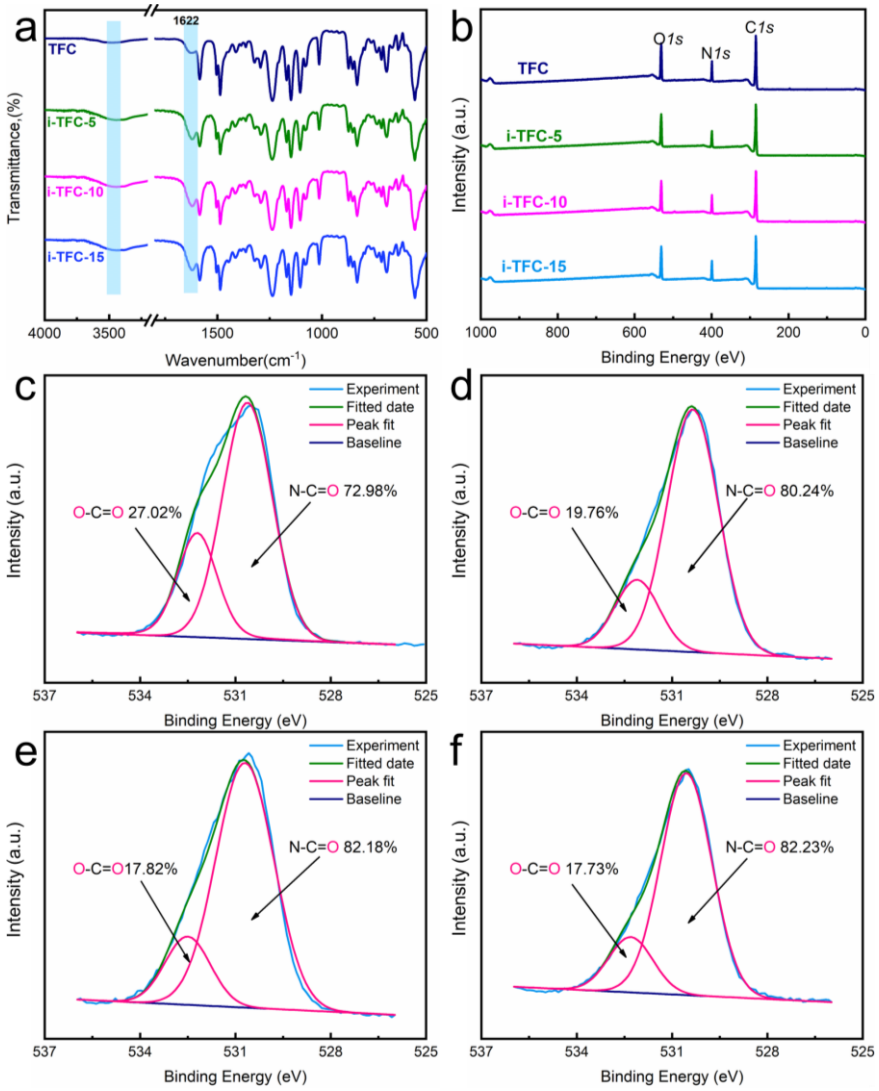

Fig. 3. (a) ATR-FTIR spectra and (b) XPS survey spectra of NF membranes with/without interlayer; XPS spectra of O1s corresponding fitting curves for (c) TFC, (d) i-TFC-5, (e) i-TFC-10, and (f) i-TFC-15

Table 1. Elemental composition of constructed membranes

Membranes	Atomic composition from XPS (%)					O/N	Degree of Network Crosslinking (%)
	C	N	O	-COOH	-N-C=O		

TFC	69.84	11.19	18.97	27.02	72.98	1.70	22.22%
i-TFC-5	71.82	10.89	17.29	19.76	80.24	1.59	31.67%
i-TFC-10	71.89	11.57	16.54	17.73	82.23	1.43	46.91%
i-TFC-15	71.37	11.85	16.78	17.82	82.18	1.42	47.94%

All TFC and i-TFC membranes exhibit negative surface charges because of the acryl chloride groups hydrolysis of unreacted TMC. The isoelectric point (IEP) of TFC membrane is pH=4.39, while the IEP for MTFC, i-TFC-5, i-TFC-10, and i-TFC-15 are pH=4.85, pH=4.88, pH=4.92, and pH=5.08, respectively (Fig. 4a and Fig. S14). The insertion of amino-containing interlayer weakens the membrane electronegativity, resulting in an increase of isoelectric point for the i-TFC membrane. The weakened electronegativity of i-TFC membranes is conducive to improving the separation selectivity of cations. It can be seen from Fig. 4b that the water contact angle values of TFC, i-TFC-5, i-TFC-10, and i-TFC-15 are 50.4° to 49.3°, 48.1°, and 39.1°, respectively, suggesting that i-TFC membranes have enhanced hydrophilicity due to the insertion of highly hydrophilic zeolite interlayer.

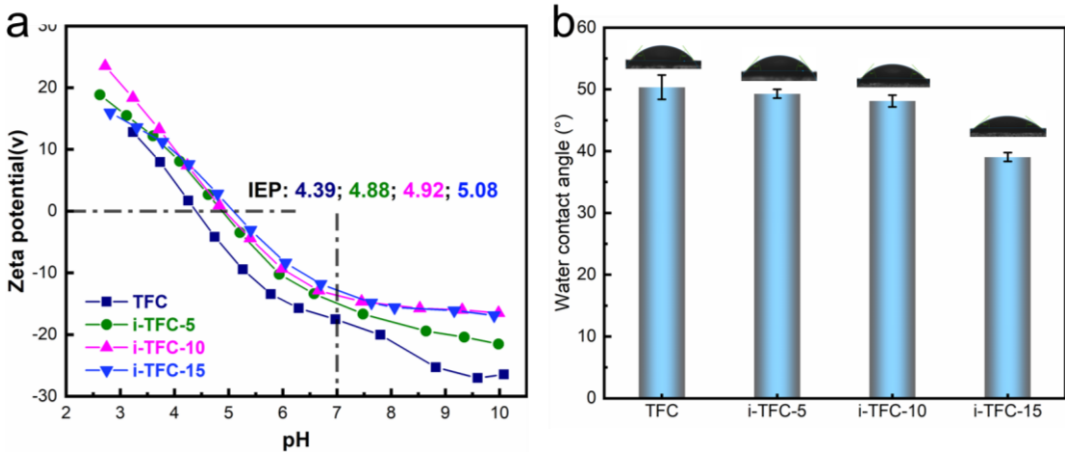

Fig. 4. (a) Surface zeta potential and (b) water contact angle for TFC, i-TFC-5, i-TFC-10, and

366 i-TFC-15 membranes

367 *3.3. Morphological characteristics and surface roughness of NF membranes*

368 Fig. 5a shows that the surface of pristine TFC membrane displays a large number of
369 nanosized nodules, which is consistent with the typical NF membranes in the literature[10,
370 44]. After introducing the zeolite interlayers, some large-sized (about 1 μm) nodules can be
371 observed in the morphology of the i-TFC-5 membrane, and partial large nodules are
372 connected (Fig. 5b). Different from the i-TFC-5 membrane, the nanoscale stripes of the
373 i-TFC-10 and i-TFC-15 membrane surfaces become thicker and rougher (Fig. 5c, d).
374 Especially, it is found that these nanoscale stripes are composed of a large number of small
375 nodules, forming a unique multi-level morphology. Particularly, the multi-level morphologies
376 consisting of nanoscale stripes increase the actual filtration area of the i-TFC membrane and
377 provide a low-resistance channel for water transport, enhancing the water permeability[10,
378 45]. SEM-Mapping results (Fig. 5e-h) demonstrate that there is no Si or Al element on the
379 i-TFC-15 membrane surface, suggesting that the zeolite nanocrystals stably exist on the
380 bottom surface of the PA layer. In addition, the increase of zeolite density on the substrate
381 contributes to an increase in the density of nanoscale stripes and ordered voids in bottom
382 surface of the PA layer, which is excellently consistent with the top surface morphology of the
383 PA layer (Fig. 6a-d). The ordered voids within the heterogeneity structures of the PA layer can
384 serve as a priority water channel and low-resistance transport path for water transport[10, 45,
385 46]. The formed multi-level heterogeneity morphology of top surface and the ordered voids of

bottom surface for the PA layer facilitate the improvement of i-TFC membrane's water permeance.

The regular variation of the top surface and bottom surface morphology for the PA layer can be explained by the aqueous template theory and diffusion variation of amine monomer(Fig. 5i)[47, 48]. The amine monomer stored on the pores of the substrate without interlayer can diffuse uniformly towards the organic phase, forming a homogeneous nodular morphology. The enhanced interaction between the substrate and the aqueous phase due to the hydrophilic zeolite interlayer makes it difficult to completely remove the aqueous phase on substrate by a rubber roller. The uneven residual aqueous solution as a soft-template on the substrate can induce the generation and evolution of 3D surface nanostructure morphology for the PA layer[47]. Meanwhile, the enhanced interaction (hydrogen bonding) caused by zeolite interlayer inhibits the diffusion of PIP monomer and creates diffusion-driven instability, which also contributes to the formation of the PA layer with 3D nanostructure surface[31]. In the short period of deposition for zeolite interlayer, amine monomer enriched in the vicinity of the discrete zeolite nanocrystal on substrates firstly reacted with TMC monomer to form the initial PA tufts. Subsequently, the slower diffusion of PIP monomer stored at the zeolite nanocrystal interface leads to a unique nanostructure in that the large-sized PA tufts are connected[49, 50]. Whereas the interlayer obtained by long-time deposition can adsorb more PIP monomers on the surface and the pore of zeolite due to the enhanced affinity of the interlayer-enhanced substrate (Fig. 2). Especially, the diffusion rate of amine monomers stored inside the pore channel is significantly lower than that of the outer surface of the

zeolite and substrates, facilitating a multilevel diffusion of amine monomers and forming a multi-level morphology NF membranes[51, 52].

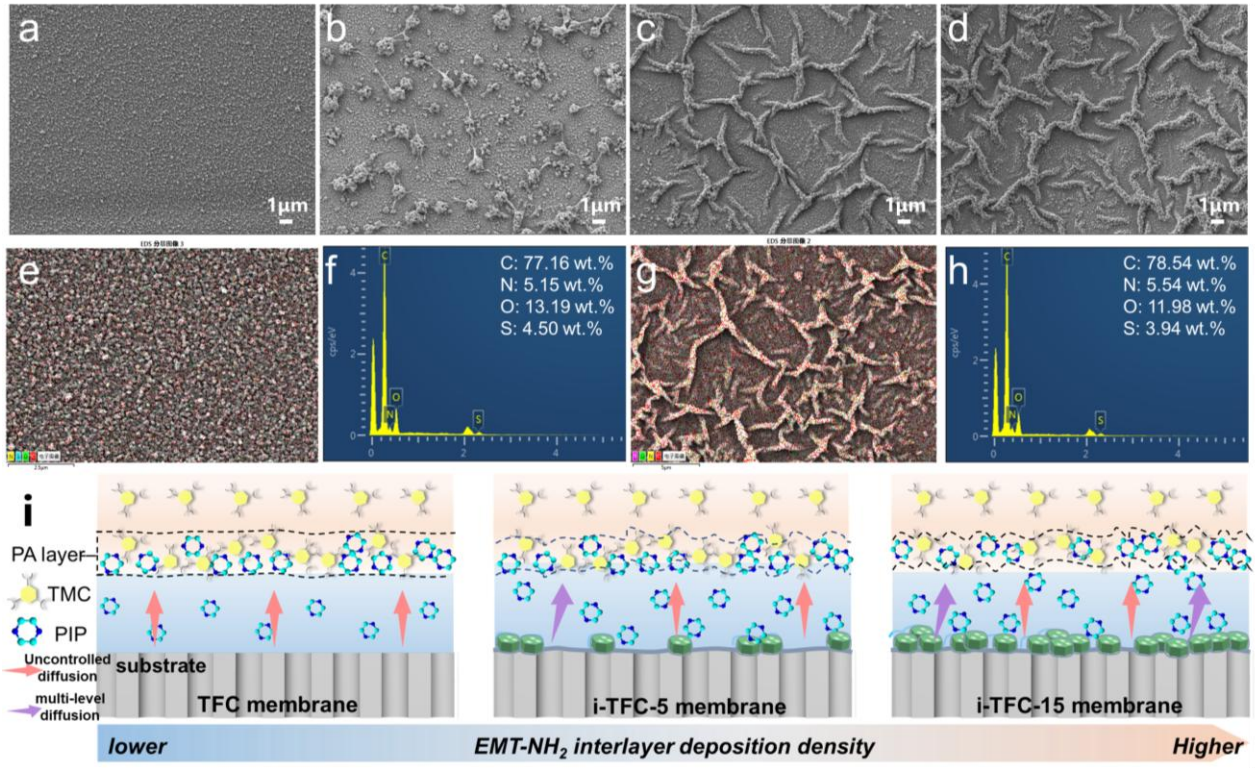

Fig. 5. Top surface SEM image of (a) TFC, (b) i-TFC-5, (c) i-TFC-10, and (d) i-TFC-15 membrane; SEM-Mapping of elemental distribution of (e) TFC and (g) i-TFC-15; EDS result of (f) TFC and (h) i-TFC-15; (i) schematic diagram of the interfacial polymerization without/with zeolite interlayer

The thickness of PA layer for the pristine TFC membrane is about 89 nm, while that of i-TFC-15 membrane with zeolite interlayer decreases to 64 nm. Constructing zeolite interlayer decreases the PA layer's thickness, which may be due to the generation of an intensive initial PA layer. The uniform distribution and increased storage for amine monomers on the MPSF-EMT substrates are prone to generating an intensive and uniform initial PA layer early in the IP process. The formed initial PA layer can restrict the further diffusion of

the amine monomer, thereby inhibiting the growth of the PA layer[42, 53]. Generally, the decreased thickness of the PA layer can shorten the water transport path and reduce the water transfer resistance, thereby improving the permeability of membrane[54]. The increased storage capacity of amine monomer on MPSF-EMT substrates was demonstrated by the UV-vis method (Fig. S15) [53]. Importantly, the relationship between PA layer thickness (δ) and the monomers diffusivity (D) was obtained in equation (7) based on the Freger model[55].

$$\delta=[L\cdot D/k(C_a\cdot f_a+C_b\cdot f_b)]^{1/3} \quad (7)$$

Where C_a and f_a are the PIP's concentration at the n-Hexane phase side of the interface and functionality of PIP, respectively. And C_b and f_b are the TMC's concentration in the organic phase and functionality of TMC, respectively. The L and k are the thickness of the diffusion boundary and the bimolecular reaction rate constant between the two monomers, respectively. Obviously, slowing down the diffusivity (D) of the monomer can reduce the thickness (δ) of PA layer. The increased storage capacity of amine monomer and the reduced diffusion jointly result in the construction of a thinner and dense PA layer. The unique multi-level morphology of the surface, ordered voids of the bottom surface, and the reduction of thickness for the PA layer jointly lead to enhanced water permeability (Fig. 6i).

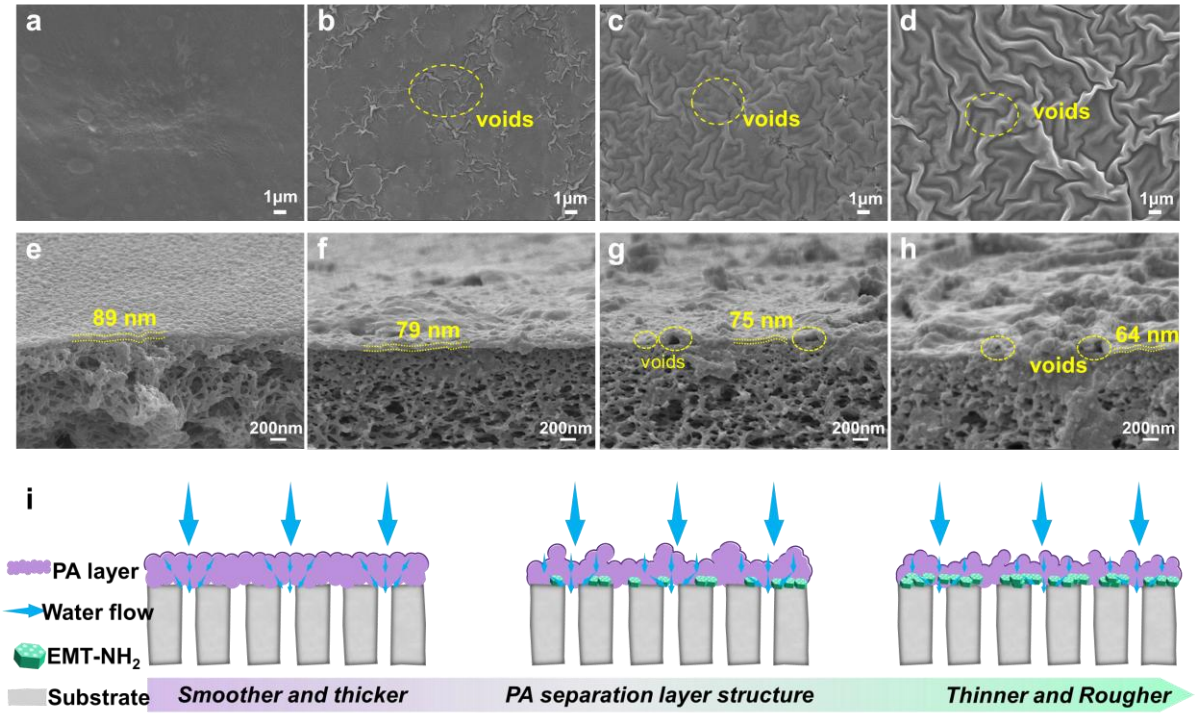

437

438 **Fig. 6.** SEM image of bottom surface morphologies for (a) TFC, (b) i-TFC-5, (c) i-TFC-10,
439 and (d) i-TFC-15 membrane; SEM image of cross-section morphologies for (e) TFC, (f)
440 i-TFC-5, (g) i-TFC-10, and (h) i-TFC-15 membrane; (i) Schematic of water transport path in
441 NF membranes without/with zeolite interlayer.

442 As seen from Fig. 7, the surface AFM image of the TFC membrane exhibits a small nodular
443 structure, while the morphologies of the i-TFC-5, i-TFC-10, and i-TFC-15 membranes depict
444 large-size nodules and nanoscale stripes, which is consistent with the SEM results. The
445 arithmetic average roughness (Ra) of the pristine TFC membrane is 10.37 nm, which indicates
446 the formation of TFC membrane with smooth flat morphology. After inserting zeolite
447 interlayer, the Ra of the i-TFC-5, i-TFC-10, and i-TFC-15 increase to 25.00, 45.40, and 45.62
448 nm, respectively. These variations demonstrated that the formed nanostructure morphology
449 caused by zeolite interlayer can enhance the roughness of membrane surface. And the
450 gradually increased roughness for the PA layer may be due to (a) the generation of large-size

nodules and nanoscale stripes in the i-TFC morphology, and (b) the existence of zeolite nanocrystals with physical sizes on substrates.

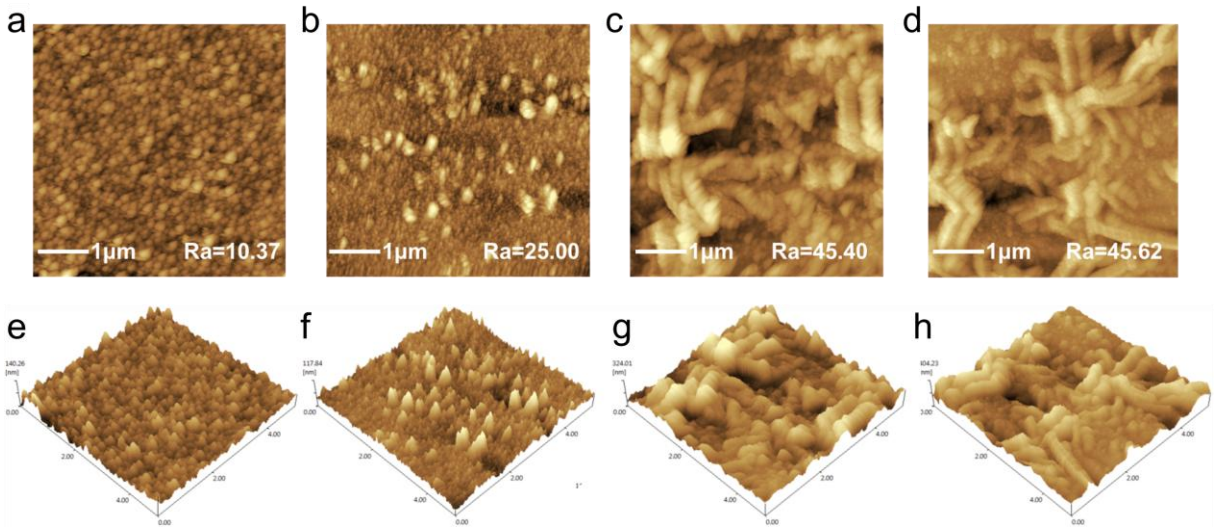

Fig. 7. AFM height 2D images of (a) TFC, (b) i-TFC-5, (c) i-TFC-10, and (d) i-TFC-15; AFM height 3D images of (a) TFC, (b) i-TFC-5, (c) i-TFC-10, and (d) i-TFC-15.

3.4 Separation performance of NF membranes

The pristine TFC membrane depicts a pure water permeance of 5.54 ± 0.26 $L \cdot m^{-2} \cdot h^{-1} \cdot bar^{-1}$ with a rejection of 97.75 ± 0.14% for Na_2SO_4 (Fig. 8a). The fabricated zeolite interlayer increases the water permeability of the i-TFC membrane, which continuously rose from 7.65 ± 0.28 to 13.82 ± 0.47 $L \cdot m^{-2} \cdot h^{-1} \cdot bar^{-1}$ with increasing interlayer deposition time from 5 h to 15 h. Such excellent performance for i-TFC membranes is mainly ascribed to the increased efficient filtration area, the reduced thickness of the PA layer, and the additional priority water channel caused by the zeolite interlayer. As seen from Fig. 8b, the i-TFC membranes with zeolite interlayer also exhibit excellent retention of divalent salts. The retentions of Na_2SO_4,

$MgSO_4$, $MgCl_2$, and $CaCl_2$ for the i-TFC-15 membrane are 98.55%, 98.42%, 97.40%, and 95.02%, respectively, which are higher than that of the controlled membrane. Fig. 8c shows that the MWCO of the TFC membrane is 266 Da, while the MWCO for the i-TFC-5, i-TFC-10, and i-TFC-15 membranes are 244, 225, and 223 Da, respectively. Compared with the controlled TFC membrane (0.375 nm), the effective pore sizes of the i-TFC-5, i-TFC-10, and i-TFC-15 membranes decrease to 0.341, 0.342, and 0.340 nm. The increased cross-linking degree of PA layer determined by XPS analysis leads to a decrease in the MWCO value and effective pore size of the i-TFC membranes[42]. The increased divalent cation selectivity for i-TFC membranes can be attributed to multiple factors. Firstly, the amino-modified substrate and insertion of the EMT-NH_2 interlayer can weaken the surface electronegativity and increases the cross-linking degree for the NF membranes, leading to higher retention ability for divalent cation. Secondly, the formed zeolite interlayer reduces the pore size of the i-TFC membrane, which further increases the retention of divalent salt (Fig. 8c)[33].

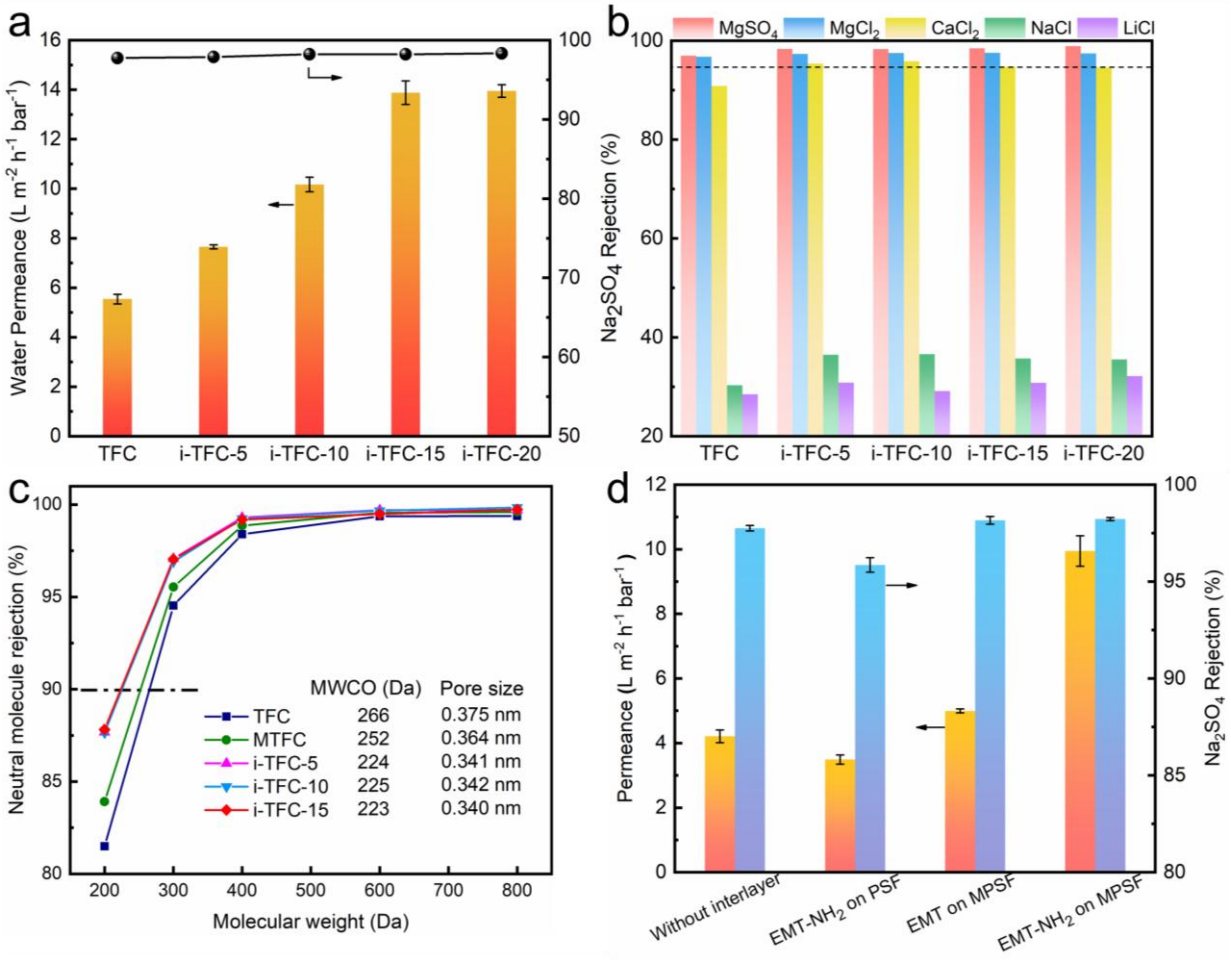

Fig. 8. (a) Water permeance and Na_2SO_4 retention of TFC and i-TFC membranes; (b) Rejection of various salts of TFC and i-TFC membranes; (c) PEG rejection curves of the various NF membranes; (d) Permeance and Na_2SO_4 retention of various NF membranes with different interlayer.

Furthermore, the relationship between the interfacial interaction of zeolite interlayer and separation performance was explored by the comparative experiments (Fig. 8d). The pure EMT-NH_2 nanocrystal on PSF substrate alone as interlayer (EMT-NH_2 on PSF) in i-TFC membrane sacrificed its permeance and selectivity, whereas the EMT nanocrystal alone as interlayer (EMT on PSF) on amino-modified PSF (MPSF) substrate in i-TFC membrane slightly improve its permeance and selectivity. It can be concluded that singly modifying

zeolite nanocrystal (or substrate surface) with amino groups tends to cause inhomogeneous interfacial forces and nanocrystal aggregation, resulting in an undesirable separation performance. The introduced amino-modified EMT-NH_2 and amino groups (EMT-NH_2 on MPSF) on the substrate surface resulted in a uniform and strong interfacial force (hydrogen bonding and covalent bonding), leading to enhanced permeance and selectivity. The better wettability of the substrate surface is usually accompanied by higher surface energy[3]. Fig. S16 depicts the wettability properties of the different interlayers. The "EMT-NH_2 on MPSF" interlayer possesses the lowest water contact angles (43.7±1.1°), which initially demonstrates that the "EMT-NH_2 on MPSF" interlayer has the best wettability and higher surface energy. Thus, it can be concluded that the excellent interfacial interaction of the zeolite nanocrystal interlayer is crucial for improving membrane performance.

As depicted in Fig. 9a, the i-TFC-15 membrane with zeolite interlayer exhibits a stable permeability and Na_2SO_4 rejection under operation conditions of 1.0 MPa and 36 h. Moreover, it can be seen from Fig. 9b that there is an approximately linear relationship between the permeability and operation pressure for all NF membranes under the operating pressure of 2.4 MPa. With the continuously increasing operating pressure, the i-TFC membranes still maintain a good linear relationship between the permeability and operation pressure (up to 2.4 MPa), which is different from that of the controlled TFC membrane. The zeolite interlayer consisting of porous and rigid zeolite can enhance the mechanical stability of the interface in the composite structure and alleviate the compression at the interface, thereby endowing the i-TFC membranes with enhanced pressure resistance[56, 57].

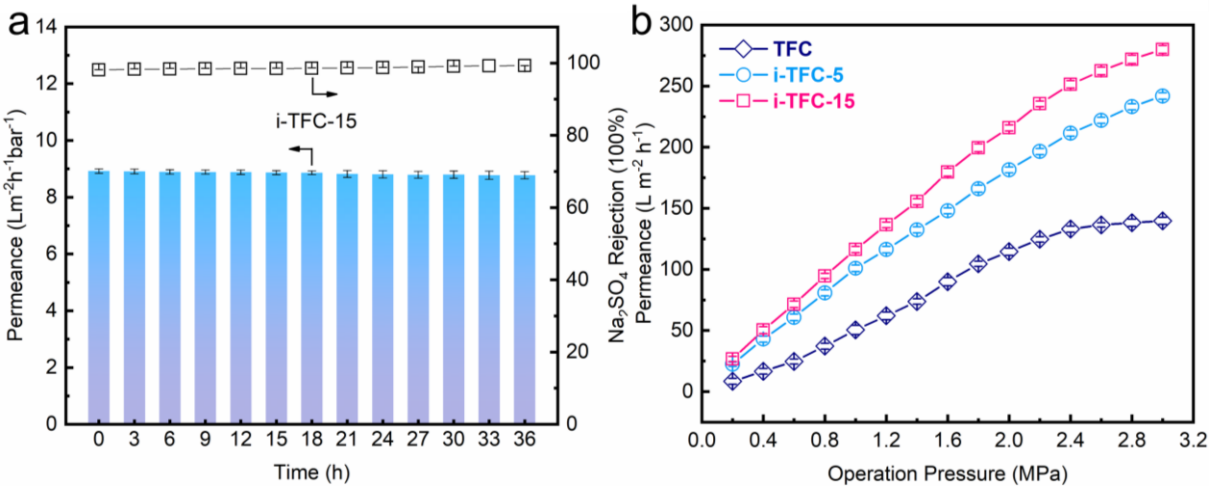

Fig. 9. (a) The performance stability of i-TFC-15 membrane (under an operating pressure of 1.0 MPa); (b) The variation of water fluxes as increased pressure for TFC, i-TFC-5, and i-TFC-15 membranes

Fig. 10 a, b depicts the water flux variation of TFC and i-TFC membranes with different depositing time interlayers by filtrating BSA solution (500 μg/g). The water fluxes of all membranes decreased to different extents with the increasing testing time. After the antifouling test with 6-h BSA, the i-TFC-15 membrane depicts a residual water flux of 60.1% (flux-decline ratio, FDR) of the initial value. The decreased water flux for the NF membrane was mainly due to the contaminants accumulation on the membrane surface and concentration polarization[58]. However, the reduced permeate can be recovered to some extent by washing the membrane surface with clean water. The flux-recovery ratio (FRR) of the i-TFC-15 membrane was 90.1%. The high FRR of i-TFC-15 membrane agreed with its structural properties. The nanoscale stripes structure of PA layer for i-TFC-15 membrane can provide a decreased fouling coverage and an optimized water transport pathway, thereby enhancing the antifouling ability of membrane, despite the fact that such nanoscale stripes would contribute

527 to greater surface roughness [59-61].

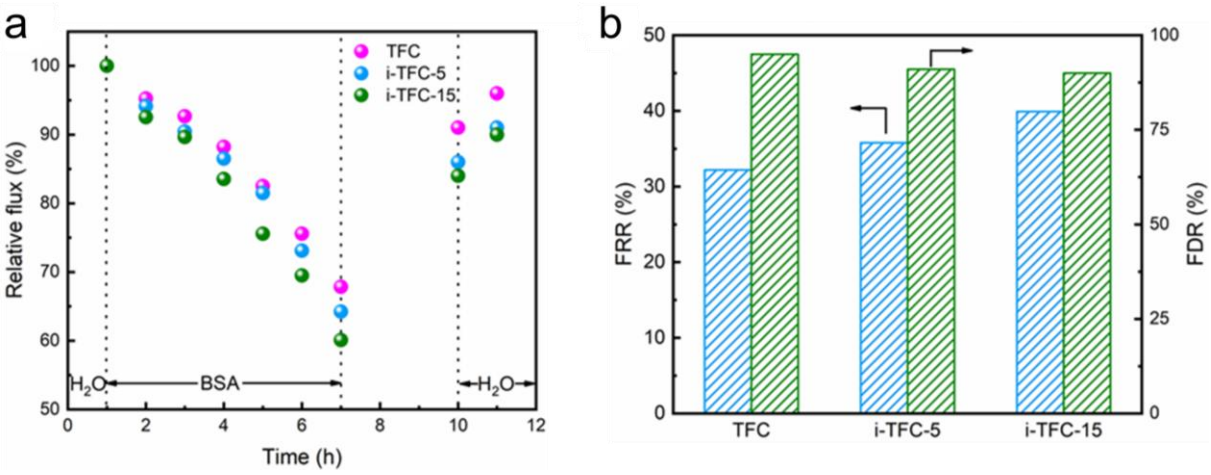

528

529 **Fig. 10.** (a) the water flux variation of TFC, i-TFC-5, and i-TFC-15 membranes by filtrating

530 BSA solution; (b) FDR and FRR of TFC, i-TFC-5, and i-TFC-15 membranes.

531 The chemical stability of TFC and i-TFC membranes after soaking both H_2SO_4 and NaOH

532 aqueous solutions were investigated and given in Fig. S18 and Fig. 11. After immersion in

533 H_2SO_4 and NaOH aqueous solutions for 24 h, the i-TFC membranes maintain their unique

534 multi-level nanostructure morphology (Fig. S17). Fig. 11 depicts that the water permeance of

535 TFC and i-TFC membranes increased significantly with increasing immersion time in H_2SO_4

536 and NaOH aqueous solutions, which was due to the poor chemical stability of

537 piperazine-based amide [62-63]. Whereas the Na_2SO_4 rejection of TFC and i-TFC membranes

538 decreased slightly as increasing immersion time. Interestingly, the i-TFC with zeolite

539 interlayer have a slower tendency of selectivity decline compared to TFC membrane,

540 suggesting that the zeolite interlayer can endow the i-TFC membranes with enhanced

541 chemical stability.

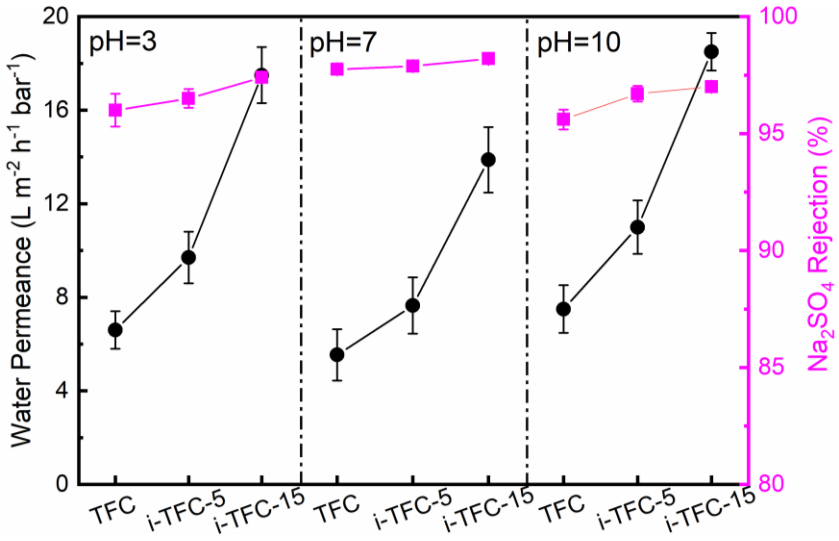

Fig. 11. Water permeance and Na_2SO_4 rejection of TFC, i-TFC-5, and i-TFC-15 membranes after immersing in different pHs (3, 7, and 10) aqueous solutions for 24 h. The pH was regulated by H_2SO_4 and NaOH.

Furthermore, the performance of the i-TFC-15 membrane with EMT-NH_2 nanocrystals interlayer was compared with other advanced NF membranes with crystalline porous materials (Fig. 12). The comparative results show that the divalent cation and divalent anion selectivity of the i-TFC-15 membrane are superior to most other TFC NF membranes composed of crystalline porous materials (MOFs, COFs, and Zeolites). Although the permeability of the i-TFC membrane is not the most desirable in the comparative membranes, its excellent pressure resistance can effectively maximize its flux in practical applications. This strategy enriches the way for enhancing the performance of NF membranes and provides more options for NF membranes in water treatment.

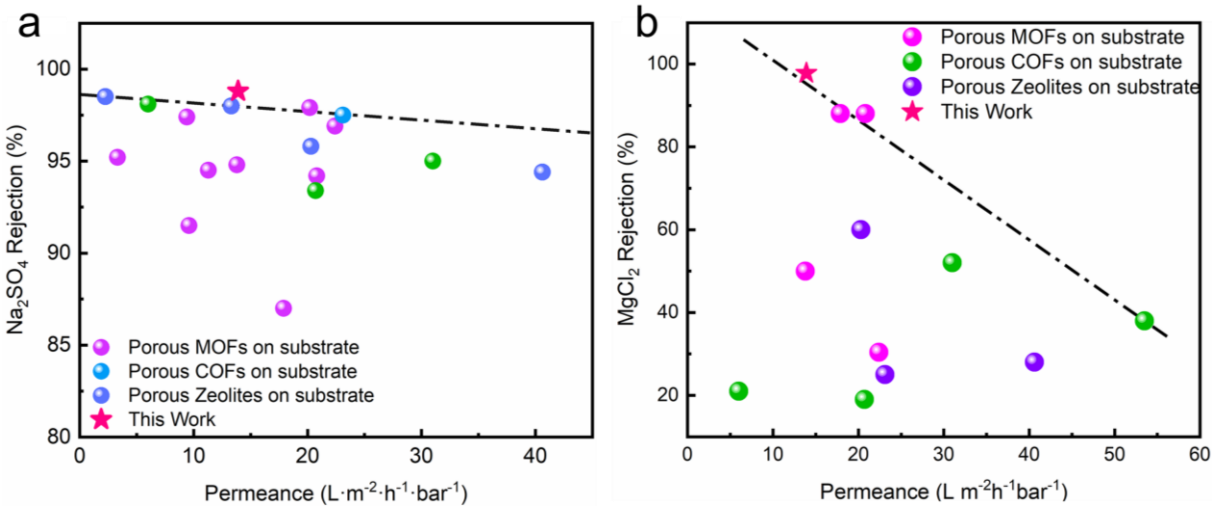

Fig. 12. Comparison of the separation performance of i-TFC membranes and other NF membranes with crystalline porous material (MOFs, COFs, and Zeolite) reported in literature (The references were listed in Tables S1).

4. Conclusions

Herein, a novel i-TFC NF membrane with excellent performance was constructed by using amino-functionalized EMT-NH_2 zeolite nanocrystals as interlayers. The hydrophilic and porous EMT-NH_2 nanocrystals optimizes the surface properties of the substrates and regulates the storage and distribution of amine monomer, facilitating the formation of a thin and dense PA layer. In addition, the residual aqueous phase as an aqueous template on substrates and the diffusion variability of amine monomer caused by the zeolite nanocrystal interlayer leads to the generation of a multi-level morphology (nanosized nodules and nanoscale stripes) for the PA layer. Compared with the controlled one, the i-TFC membrane with EMT-NH_2 interlayer exhibited a superior water permeability (2.5 times that of the controlled one) and an excellent rejection of divalent salt. Meanwhile, the rigid hydrophilic zeolite interlayer endowed the i-TFC membrane with excellent pressure resistances (up to 2.4 MPa), long-term operation

stability, and antifouling propensity (flux-recovery-ratio, 90.1%). This study provides an effective strategy to construct a novel NF membrane with excellent separation performance.

Acknowledgements

This work was financially supported by National Key Research and Development Program of China of Ministry of Science and Technology (2022YFE0116000), National Natural Science Foundation of China (No. U2006230. No. 22175200, No. 21975285), and Fujian Province Science and Technology Program, Innovation Fund (2022C0021).

References

[1] J.M. Gohil, P. Ray, A review on semi-aromatic polyamide TFC membranes prepared by interfacial polymerization: Potential for water treatment and desalination, Sep. Purif. Technol. 181 (30) (2017) 159-182, https://doi.org/10.1016/j.seppur.2017.03.020.

[2] X. Huggins, T. Gleeson, M. Kummu, S. C. Zipper, Y. Wade, T. J. Troy, J. S. Famiglietti, Hotspots for social and ecological impacts from freshwater stress and storage loss, Nat. Commun. 13 (1) (2022) 439, https://doi.org/10.1038/s41467-022-28029-w.

[3] B. Yuan, S. Zhao, P. Hu, J. Cui, Q.J. Niu, Asymmetric polyamide nanofilms with highly ordered nanovoids for water purification, Nat. Commun. 11 (1) (2020) 6102, https://doi.org/10.1038/s41467-020-19809-3.

[4] W. J. Lau, A. F. Ismail, N. Misdan, M. A. Kassim, A recent progress in thin film composite membrane: A review, Desalination 287 (2012) 190-199, https://doi.org/10.1016/j.desal.2011.04.004.

[5] Z. Yang, H. Guo, C. Y. Y. Tang, The upper bound of thin-film composite (TFC) polyamide membranes for desalination, J. Membr. Sci. 590 (2019) 117297, https://doi.org/10.1016/j.memsci.2019.117297.

[6] K. Wang, X. Wang, B. Januszewski, Y. Liu, D. Li, R. Fu, M. Elimelech, X. Huang, Tailored design of nanofiltration membranes for water treatment based on synthesis-property-performance relationships, Chem. Soc. Rev. 51 (2) (2021) 672-719,

https://doi.org/10.1039/D0CS01599G.

[7] D. Zhao, F. Fang, L. Shen, Z. Huang, Q. Zhao, H. Lin, T. Chung, Engineering metal–organic frameworks (MOFs) based thin-film nanocomposite (TFN) membranes for molecular separation, Chem. Eng. J. 454 (3, 15) (2023) 1404747, https://doi.org/10.1016/j.cej.2022.140447.

[8] L. Lin, R. Lopez, G.Z. Ramon, O. Coronell, Investigating the void structure of the polyamide active layers of thin-film composite membranes, J. Membr. Sci. 497 (1) (2016) 365-376, https://doi.org/10.1016/j.memsci.2015.09.020.

[9] S. Zhao, K. Chen, Y. Niu, B. Yuan, C. Jiang, M. Wang, P. Li, Y. Hou, H. Sun, D. Xia, Q. J. Niu, Heterogeneous polyamide composite membranes based on aromatic poly(amidoamine) dendrimer for molecular sieving, J. Membr. Sci. 671 (5) (2023) 121384, https://doi.org/10.1016/j.memsci.2023.121384.

[10] Z. Tan, S. Chen, X. Peng, L. Zhang, C. Gao, Polyamide membranes with nanoscale Turing structures for water purification, Science 360 (6388) (2018) 518-521, https://doi.org/10.1126/science.aar6308.

[11] B. Khorshidi, B. Soltannia, T. Thundat, M. Sadrzadeh, Synthesis of thin film composite polyamide membranes: Effect of monohydric and polyhydric alcohol additives in aqueous solution, J. Membr. Sci. 523 (1) (2017) 336-345, https://doi.org/10.1016/j.memsci.2016.09.062.

[12] P. Hu, J. He, B. Tian, Z. Xu, T. Yuan, H. Sun, P. Li, Q. J. Niu, Application of diazonium-induced anchoring process on ultrafiltration substrate for the fabrication of nanofiltration membrane with enhanced desalination performance, Desalination 496 (15) (2021) 114340, https://doi.org/10.1016/j.desal.2020.114340.

[13] Y.S. Khoo, W.J. Lau, Y.Y. Liang, N. Yusof, A.F. Ismail, Surface modification of PA layer of TFC membranes: Does it effective for performance Improvement?, J. Ind. Eng. Chem. 102 (25) (2021) 271-292, https://doi.org/10.1016/j.jiec.2021.07.006.

[14] Z. Yang, P. Sun, X. Li, B. Gan, L Wang, X. Song, H.D. Park, C.Y. Tang, A Critical Review on Thin-Film Nanocomposite Membranes with Interlayered Structure: Mechanisms, Recent Developments, and Environmental Applications, Environ. Sci. Technol. 54 (24) (2021) 15563-15583, https://doi.org/10.1016/j.memsci.2022.120952.

[15] G. Gong, P. Wang, Z. Zhou, Y. Hu, New Insights into the Role of an Interlayer for the Fabrication of Highly Selective and Permeable Thin-Film Composite Nanofiltration Membrane, ACS Appl. Mater. Interfaces 11 (7) (2019) 7349-7356, https://doi.org/10.1021/acsami.8b18719.

[16] C. Ji, Z. Zhai, C. Jiang, P. Hu, S. Zhao, S. Xue, Z. Yang, T. He, Q. J. Niu, Recent advances in high-performance TFC membranes: A review of the functional interlayers, Desalination 500 (15) (2021) 114869. https://doi.org/10.1016/j.desal.2020.114869.

[17] S. Karan, Z. Jiang, A.G. Livingston, Sub-10 nm polyamide nanofilms with ultrafast solvent transport for molecular separation, Science 348 (6241) (2015) 1347-1351, https://doi.org/10.1126/science.aaa5058.

[18] Y. Guo, C. Ji, Y. Ye, Y Chen, Z. Yang, S. Xue, Q. J. Niu, High performance nanofiltration membrane using self-doping sulfonated polyaniline, J. Membr. Sci. 652 (15) (2022) 120441, https://doi.org/10.1016/j.memsci.2022.120441.

[19] M.Q. Seah, W.J. Jye, P. S. Goh, A.F. Ismail, Greener synthesis of functionalized-GO incorporated TFN NF membrane for potential recovery of saline water from salt/dye mixed solution, Desalinaiton 523 (1) (2021) 115403, https://doi.org/10.1016/j.desal.2021.115403.

[20] H. Lan, Y. Zhai, K. Chen, Z. Zhai, C. Jiang, P. Li, Y. Hou, Q. J. Niu, Fabrication of high performance nanofiltration membrane by construction of Noria based nanoparticles interlayer, Sep. Purif. Technol. 290 (1) (2022) 120781, https://doi.org/10.1016/j.seppur.2022.120781.

[21] Z. Yang, F. Wang, H. Guo, L. Peng, X. Ma, X. Song, Z. Wang, C.Y. Tang, Mechanistic Insights into the Role of Polydopamine Interlayer toward Improved Separation Performance of Polyamide Nanofiltration Membranes, Environ. Sci. Technol. 54 (18) (2020) 11611-11621, https://doi.org/10.1021/acs.est.0c03589.

[22] J. Zhu, L. Qin, A. Uliana, J. Hou, J. Wang, Y. Zhang, X. Li, S. Yuan, J. Li, M. Tian, Elevated Performance of Thin Film Nanocomposite Membranes Enabled by Modified Hydrophilic MOFs for Nanofiltration, ACS Appl. Mater. Interfaces 9 (2) (2017) 1975-1986, https://doi.org/10.1021/acsami.6b14412.

[23] W.J. Lau, S. Gray, T. Matsuura, D. Emadzadeh, J. Chen, A.F. Ismail, A review on polyamide thin film nanocomposite (TFN) membranes: History, applications, challenges and approaches, Water Res. 80 (1) (2015) 306-324. https://doi.org/10.1016/j.watres.2015.04.037.

[24] D.S. Dlamini, B.B. Mamba, J. Li, The role of nanoparticles in the performance of nano-enabled composite membranes-A critical scientific perspective, Sci. Total Environ. 656 (15) (2019) 723-731, https://doi.org/10.1016/j.scitotenv.2018.11.421.

[25] P. Li, M. Zhang, Z. Zhai, M. Wang, P. Li, Y. Hou, Q.J. Niu, Precise assembly of a zeolite imidazolate framework on polypropylene support for the fabrication of thin film

667 nanocomposite reverse osmosis membrane, J. Membr. Sci. 612 (15) (2020) 118412,
668 https://doi.org/10.1016/j.memsci.2020.118412.
669 [26] K. Chen, P. Li, H. Zhang, H. Sun, X. Yang, D. Yao, X. Pang, X. Han, Q.J. Niu, Organic
670 solvent nanofiltration membrane with improved permeability by *in-situ* growth of
671 metal-organic frameworks interlayer on the surface of polyimide substrate, Sep. Purif.
672 Technol. 251 (15) (2020) 117387, https://doi.org/10.1016/j.seppur.2020.117387.
673 [27] M. Ding, X. Cai, H. Jiang, Improving MOF stability: approaches and applications, Chem.
674 Sci. 10 (44) (2019) 10209-10230, https://doi.org/10.1039/C9SC03916C.
675 [28] G. Cai, P. Yan, L. Zhang, H. Zhou, H. Jiang, Metal-Organic Framework-Based
676 Hierarchically Porous Materials: Synthesis and Applications, Chem. Rev. 121 (20) (2021)
677 12278-12326, https://doi.org/10.1021/acs.chemrev.1c00243.
678 [29] D. Wang, M. Tian, S. Han, K. Ding, L. Yin, J. Zhu, Y. Zhang, L. Han, Enhanced
679 performance of thin-film nanocomposite membranes achieved by hierarchical zeolites for
680 nanofiltration, J. Membr. Sci. 671 (5) (2023) 121405,
681 https://doi.org/10.1016/j.memsci.2023.121405.
682 [30] E.P. Ng, D. Chateigner, T. Bein, V. Valtchev, S. Mintova, Capturing Ultrasmall EMT
683 Zeolite from Template-Free Systems, Science 335 (6064) (2012) 70-73,
684 https://doi.org/10.1126/science.1214798.
685 [31] S. Han, J. Zhu, A.A. Uliana, D. Li, Y. Zhang, L. Zhang, Y. Wang, T. He, M. Elimelech,
686 Microporous organic nanotube assisted design of high performance nanofiltration
687 membranes, Nat. Commun. 13 (1) (2022) 7954,
688 https://doi.org/10.1038/s41467-022-35681-9.
689 [32] L. Bai, Y. Liu, A. Ding, N. Ren, G. Li, H. Liang, Fabrication and characterization of
690 thin-film composite (TFC) nanofiltration membranes incorporated with cellulose
691 nanocrystals (CNCs) for enhanced desalination performance and dye removal, Chem.
692 Eng. J. 358 (15) (2019) 1519-1528, https://doi.org/10.1016/j.cej.2018.10.147.
693 [33] S. Singh, K.C. Khilbe, T. Matsuura, P. Ramanurthy, Membrane characterization bu solute
694 transport and atomic free microscopy, J. Membr. Sci. 142 (1, 2) (1998) 111-127,
695 https://doi.org/10.1016/S0376-7388(97)00329-3.
696 [34] X. Wu, J. Tammer, D. Ng, D. Acharya, Z. Xie, Sewage concentration via a graphene
697 oxide modified thin-film nanocomposite forward osmosis membrane: Enhanced
698 performance and mitigated fouling, Chem. Eng. J. 420 (2, 15) (2021) 127718,
699 https://doi.org/10.1016/j.cej.2020.127718.
700 [35] Y. Zhu, J. Wang, F. Zhang, S. Gao, A. Wang, W. Fang, J. Jin, Zwitterionic Nanohydrogel

Grafted PVDF Membranes with Comprehensive Antifouling Property and Superior Cycle Stability for Oil-in-Water Emulsion Separation, Adv. Funct. Mater. 28 (40) (2018) 1804121, https://doi.org/10.1002/adfm.201804121.

[36] Q. Zhang, H. Guo, G. Muradi, B. Zhang, Tuning the Multi-Scale Structure of Mixed-Matrix Membranes for Upgrading CO_2 Separation Performances, Sep. Purif. Technol. 293 (15) (2022) 121118, https://doi.org/10.1016/j.seppur.2022.121118.

[37] H. Younesi, S, Asghari, G.F. Pasha, M. Tajbakhsh, Ugi-modified nano NaY zeolite for the synthesis of new 1,5-dihydro-2H-pyrrol-2-ones under mild conditions, Appl. Organomet Chem. 37 (7) (2023) e7127, https://doi.org/10.1002/aoc.7127.

[38] E.P. Ng, H. Awala, K.H. Tan, F. Adam, R. Retoux, S. Mintova, EMT-type zeolite nanocrystals synthesized from rice husk, Microporous Mesoporous Mater. 204 (1) (2015) 204-209. https://doi.org/10.1016/j.micromeso.2014.11.017.

[39] W. Liang, J. Huang, P. Xiao, R. Singh, J. Guo, L. Dehdari, G. Li, Amine-immobilized HY zeolite for CO2 capture from hot flue gas, Chin. J. Chem. Eng. 43 (2022) 335-342, https://doi.org/10.1016/j.cjche.2022.02.004.

[40] Z. Salmi, K. Benzarti, M.M. Chehimi, Diazonium Cation-Exchanged Clay: An Efficient, Unfrequented Route for Making Clay/Polymer Nanocomposites, Langmuir 29 (44) (2013) 13323-13328, https://doi.org/10.1021/la402710r.

[41] Z. Liu, L. Zhao, H. Ye, Z. Wang, Y. Chen, Y. Li, L. Liu, Y. Guo, Y. Chen, Q. Jason. Niu, Highly anions-selective polyamide nanofiltration membrane fabricated by rod-coating assisted interfacial polymerization, J. Membr. Sci. 668 (15) (2023) 121273, https://doi.org/10.1016/j.memsci.2022.121273.

[42] K. Chen, S. Zhao, H. Lan, T. Xie, H. Wang, Y. Chen, P. Li, H. Sun, Q. Jason. Niu, Dual-electric layer nanofiltration membranes based on polyphenol/PEI interlayer for highly efficient Mg^{2+}/Li^{+} separation, J. Membr. Sci. 660 (15) (2022) 120860, https://doi.org/10.1016/j.memsci.2022.120860.

[43] C.Y. Tang, Y.N. Kwon, J.O. Leckie, Probing the nano- and micro-scales of reverse osmosis membranes-A comprehensive characterization of physiochemical properties of uncoated and coated membranes by XPS, TEM, ATR-FTIR, and streaming potential measurements, J. Membr. Sci. 287 (1, 5) (2007) 146-156, https://doi.org/10.1016/j.memsci.2006.10.038.

[44] G. Xu, Z. An, M. Wang, K. Xu, H. Zhao, Q. Liu, Polyamide layer modulation for

PA-TFC membranes Optimization: Developments, Mechanisms, and implications, Sep. Purif. Technol. 311 (15) (2023) 123200, https://doi.org/10.1016/j.seppur.2023.123200.
[45] S. Shao, F. Zeng, L. Long, X. Zhu, L. E. Peng, F. Wang, Z. Yang, C.Y. Tang, Nanofiltration Membranes with Crumpled Polyamide Films: A Critical Review on Mechanisms, Performances, and Environmental Applications, Environ. Sci. Technol. 56 (18) (2022) 12811-12827, https://doi.org/10.1021/acs.est.2c04736.
[46] Y. Hu, F. Wang, Z. Yang, C.Y. Tang, Modeling nanovoid-enhanced water permeance of thin film composite membranes, J. Membr. Sci. 675 (5) (2023) 121555, https://doi.org/10.1016/j.memsci.2023.121555.
[47] C. Jiang, L. Tian, Z. Zhai, Y. Shen, W. Dong, M. He, Y. Hou, Q.J. Niu, Thin-film composite membranes with aqueous template-induced surface nanostructures for enhanced nanofiltration, J. Membr. Sci. 589 (1) (2019) 117244, https://doi.org/10.1016/j.memsci.2019.117244.
[48] F. Gao, H. Liu, Y. Zhang, D. Liu, Z. Xie, W. Peng, Y. Song, R. Hu, D. Chen, J. Kang, R. Xu, Y. Cao, M. Xiang, Polyamide membrane with nanoscale stripes and internal voids for high-performance nanofiltration, J. Membr. Sci. 671 (5) (2023) 121406, https://doi.org/10.1016/j.memsci.2023.121406.
[49] Z. Guo, H. Wang, L. Wang, B. Zhao, Y. Qian, H. Zhang, Polyamide thin-film nanocomposite membrane containing star-shaped ZIF-8 with enhanced water permeance and PPCPs removal, Sep. Purif. Technol. 292 (1) (2022) 120886, https://doi.org/10.1016/j.seppur.2022.120886.
[50] J. Zhu, J. Hou, S. Yuan, Y. Zhao, Y. Li, R. Zhang, M. Tian, J. Li, J. Wang, B.V.B. Bruggen, MOF-positioned polyamide membranes with a fishnet-like structure for elevated nanofiltration performance, J. Mater. Chem. A 7 (27) (2019) 16313-16322, https://doi.org/10.1039/C9TA02299F.
[51] X. Zhu, Z. Yang, Z. Gan, X. Cheng, X. Tang, X. Luo, D. Xu, G. Li, H. Liang, Toward tailoring nanofiltration performance of thin-film composite membranes: Novel insights into the role of poly(vinyl alcohol) coating positions, J. Membr. Sci. 614 (15) (2020) 118526, https://doi.org/10.1016/j.memsci.2020.118526.
[52] P. Hu, B. Tian, Z. Xu, Q.J. Niu, Fabrication of high performance nanofiltration membrane on a coordination-driven assembled interlayer for water purification. Sep. Purif. Technol. 235 (18) (2020) 116192, https://doi.org/10.1016/j.seppur.2019.116192.
[53] Y. Chen, H. Sun, S. Tang, H. Feng, H. Zhang, K. Chen, P. Li, Q.J. Jason, Nanofiltration membranes with enhanced performance by constructing an interlayer integrated with

767 dextran nanoparticles and polyethyleneimine coating, J. Membr. Sci. 654 (15) (2022)
768 120537, https://doi.org/10.1016/j.memsci.2022.120537.
769 [54] X. You, H. Wu, R. Zhang, Y. Su, L. Cao, Q. Yu, J. Yuan, K. Xiao, M. He, Z. Jiang,
770 Metal-coordinated sub-10 nm membranes for water purification, Nat. Commun. 11 (1)
771 (2019) 4160, http://dx.doi.org/10.1038/s41467-019-12100-0.
772 [55] V. Freger, Nanoscale Heterogeneity of Polyamide Membranes Formed by Interfacial
773 Polymerization, Langmuir 19 (11) (2003) 4791-4797,
774 http://dx.doi.org/10.1021/la020920q.
775 [56] M. Yasukawa, S. Mishima, Y. Tanaka, T. Takahashi, H. Matsuyama, Thin-film composite
776 forward osmosis membrane with high water flux and high pressure resistance using a
777 thicker void-free polyketone porous support, Desalination 402 (16) (2017) 1-9,
778 https://doi.org/10.1016/j.desal.2016.09.017.
779 [57] S. Xue, C. Lin, C. Ji, Y. Guo, L. Liu, Z. Yang, S. Zhao, X. Cai, Q.J. Jason, R.B. Kaner,
780 Thin-Film Composite Membranes with a Hybrid Dimensional Titania Interlayer for
781 Ultrapermeable Nanofiltration, Nano Letter 22 (3) (2022) 1039-1046,
782 https://doi.org/10.1021/acs.nanolett.1c04000.
783 [58] H. Yu, L. Xu, Y. Luo, M. Guo, X. Yan, X. Jiang, L. Yu, Preparation of highly permeable
784 and selective nanofiltration membranes with antifouling properties by introducing the
785 capsaicin derivative into polyamide thin selective layer by bidirectional interfacial
786 polymerization, J. Membr. Sci. 675 (5) (2020) 121569,
787 https://doi.org/10.1016/j.memsci.2023.121569.
788 [59] D. Rana, T. Matsuura, Surface Modifications for Antifouling Membranes, Chem. Rev.
789 110 (4) (2010) 2448-2471, https://doi.org/10.1021/cr800208y.
790 [60] W. Shang, F. Sun, W. Jia, J. Guo, S. Yin, P.W. Wong, A.K. An, High-performance
791 nanofiltration membrane structured with enhanced stripe nano-morphology, J. Membr.
792 Sci. 600 (15) (2020) 117852, https://doi.org/10.1016/j.memsci.2020.117852.
793 [61] Q. Gan, C. Wu, L. Long, l.E. Peng, Z. Yang, H. Guo, C.Y.Y. Tang, Does Surface
794 Roughness Necessarily Increase the Fouling Propensity of Polyamide Reverse Osmosis
795 Membranes by Humic Acid?, Environ. Sci. Technol. 57 (6) (2023) 1548-2556,
796 https://doi.org/10.1021/acs.est.2c07872.
797 [62] B.M. Jun, S.H. Kim, S.K. Kwak, Y.N. Kwan, Effect of acidic aqueous solution on
798 chemical and physical properties of polyamide NF membranes, Appl. Surf. Sci. 444 (30)
799 (2018) 387-398. https://doi.org/10.1016/j.apsusc.2018.03.078.
800 [63] Y. Wang, S.J.D. Smith, Y. Liu, P. Lu, X. Zhang, D. Ng, Z. Xie, Surface hydrophilicity

modification of thin-film composite membranes with metal-organic frameworks (MOFs) Ti-UiO-66 for simultaneous enhancement of anti-fouling property and desalination performance, Sep. Purif. Technol. 302 (1) (2022) 122001. https://doi.org/10.1016/j.seppur.2022.122001.